analytical chemistry

Article

pubs.acs.org/ac

Fast Chemical Imaging at High Spatial Resolution by Laser Ablation Inductively Coupled Plasma Mass Spectrometry

Hao A. O. Wang,[†,‡] Daniel Grolimund,[*,‡] Charlotte Giesen,[§] Camelia N. Borca,[‡] James R. H. Shaw-Stewart,[⊥,∥,▽] Bernd Bodenmiller,[§] and Detlef Günther[*,†]

[†]Trace Element and Micro Analysis Group, ETH Zürich, Wolfgang-Pauli-Str. 10, 8093 Zurich, Switzerland

[‡]microXAS Beamline Project, Swiss Light Source, Paul Scherrer Institute, 5232 Villigen PSI, Switzerland

[§]Institute of Molecular Life Sciences, University of Zurich, 8057 Zurich, Switzerland

[⊥]Materials Group, General Energies Department, Paul Scherrer Institute, 5232 Villigen PSI, Switzerland

[∥]Laboratory for Functional Polymers, EMPA, 8600 Dübendorf, Switzerland

Supporting Information

ABSTRACT: In recent years, chemical imaging was prognosticated to become one of the key analytical applications for laser ablation inductively coupled plasma mass spectrometry (LA-ICP-MS). However, moderate spatial resolution and the associated measurement time required for a larger sampling area, have restricted this versatile, high sensitivity technique from being routinely used in two-dimensional chemical imaging. This work describes the development and investigation of a low dispersion sample chamber (tube cell), which allows improvement of the imaging capabilities by reduction of the single LA shot duration to 30 ms (full width at 1% maximum). The new tube cell is based on a constant laminar flow and a well-controlled delivery of the laser-ablated aerosol into the transport system, leading to minimized tailing of the aerosol washout and helping to separate the signals even at repetition rates as high as 20−30 Hz. To demonstrate the improved imaging capabilities, microstructured metallic thin film patterns were analyzed at a spatial resolution of a few micrometers. The LA-ICP-MS results obtained were comparable to Synchrotron-based micro-X-ray fluorescence (SR-microXRF). The suitability of the newly designed cell for multielement acquisitions was demonstrated using a simultaneous ICP-Mattauch−Herzog-MS. Finally, the novel laser ablation cell was applied to image the distribution of a metal-tagged biomarker in a thin section of breast cancer tissue. This application demonstrates that the technique is able to produce subcellular (~1 μm) spatial resolution, which is crucial for morphological assessment in cancer diagnostics.

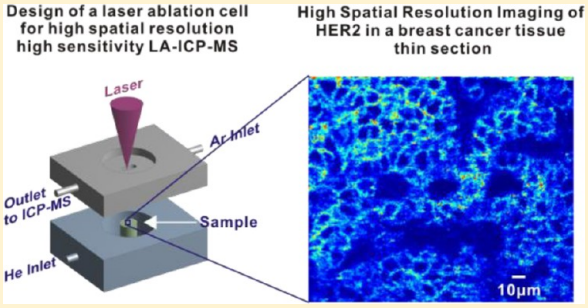

INTRODUCTION

LA-ICP-MS Imaging. Laser ablation (LA) was first coupled to inductively coupled plasma mass spectrometry (ICP-MS) in 1985.[1] Despite the nature of a focused laser beam, initial analyses were concentrated on homogeneous bulk samples to evaluate the capabilities of this technique. As a direct solid sampling method, LA-ICP-MS provides accurate quantitative information on major, minor, trace, and ultratrace elements of industrial, geological, environmental, and biological samples.[2] Because essential properties of samples are frequently related to the spatial distributions of elements, analytical techniques capable of imaging are highly advantageous, and a number of attempts have been made to use LA-ICP-MS as an elemental imaging technique. In an early example of imaging geological samples, Chenery et al. measured the gold distribution in sulfide minerals using a ~20 μm laser spot, recording discrete two-dimensional distribution patterns, complemented by depth profiles.[3] Imaging of two environmental samples using LA-ICP-MS was described by Woodhead et al. Sr isotopic images were obtained on a 4.8 mm^2 area of a barramundi otolith with a 71 μm laser spot, and multi-trace-element maps were recorded on a stalagmite sample with a larger laser spot size of 157 μm.[4] For biological tissue imaging, an early study by Kindness et al. demonstrated the feasibility of a LA-ICP-time-of-flight-MS (LA-ICP-TOF-MS). Trace elements of Cu and Zn in a sheep liver thin section were acquired in raster imaging mode using a 10 μm laser beam. Multiple laser shots were acquired at one position, before moving the sample 300 μm to the next position. Between ablation of adjacent positions, tens of seconds were used for the washout of the aerosol.[5] Furthermore, a 2D image of a brain section was presented by Hutchinson et al. on a 100 mm^2 area using parallel ~1 Hz line scans acquired in about 7 h.[6] Later, Jackson et al. showed multi-isotope images of a 10 mm^2 area on a rat brain section with a spatial resolution of >60 μm obtained in 2 h.[7] Becker et al. illustrated the distribution of seven isotopes within a human

Received: April 4, 2013
Accepted: August 18, 2013
Published: August 18, 2013

brain section at 20 Hz ablation frequency based on parallel line scans with 50 μm laser spot size.[8]

Some of the studies utilizing low sampling rate considered the significant laser-ablated aerosol dispersion, while others employing high-frequency ablation generated "finer" images more efficiently at the expense of spatial resolution. Most of the studies mentioned showed an *effective* spatial resolution of approximately 100 μm. The *effective* spatial resolution is determined by the laser spot size convoluted by the system dispersion resulting from washout time and the scanning speed. For these early studies, within a typical measurement time between 1 and 2 h, only a limited number of approximately 40 × 40 *spatially* resolved pixels could be measured due to the aerosol washout times of their transport systems estimated to be on the order of a few seconds. Therefore the limited data acquisition speed restricts the recordable total number of pixels and, as a result, the resolution and quality of an image. However many analytical applications would greatly benefit from higher resolution, such as contaminant migration in geological samples, climate research from trace element distribution in stalagmites, or a diagnostic analysis of a biological specimen. Furthermore, most of the chemical images recorded by LA-ICP-MS so far have been based on sequential ion detection instruments, for example, quadrupole mass analyzers and single collector sector field mass analyzers. However, such mass analyzer systems are clearly disadvantageous for multi-isotope imaging based on short single laser pulses, since the loss of all other mass-to-charge-ratio (m/Q) ions during integration of one m/Q cannot be avoided.

Consequently the trade-off among spatial resolution, sampling time, sampling area, and number of sampling isotopes represents a limitation for imaging using LA-ICP-MS. It must be noted that an increase in laser ablation frequency or a decreased scan speed resulting in denser ablation spots does not improve the spatial resolution of images because the aerosol washout time after each laser shot and the laser spot size become the limiting factors. At higher laser repetition rates, the signal overlap between adjacent shots becomes more important. This problem can only be solved by developing either mathematical postacquisition deconvolution methods[9] or faster washout LA cells. The latter as a direct technical solution is more favorable because it provides raw data free of dispersion artifacts and can be routinely applicable.

LA-ICP-MS Ablation Cell Development. Many laser ablation cells have been developed with the aim of a fast washout and a high transport efficiency.[10] However, short washout time is not the only goal of cell development since the cell also needs to be large enough to host different sample geometries as well as simple enough to be manufactured with reasonable technical effort. The fastest aerosol washout time has been reported for in-torch ablation, where Tanner et al. placed the sample directly in the ICP torch. This resulted in single shot signal durations of a few milliseconds.[11−13] However, this sampling strategy is limited to very small samples and does not allow imaging, since the precise two-dimensional movement of the sample is difficult to realize and commercial LA systems are not equipped with a moveable laser beam. Nevertheless, this study can be considered as a benchmark for the optimization of external ablation cells.

Three different design principles are commonly found in fast washout cells. As an example of the first design principle, Leach et al. presented different cells based on aerosol ejection direction parallel to that of the carrier gas with various cell volumes.[14] Pisonero et al. demonstrated a "high efficiency aerosol dispersion" cell (HEAD cell) by extracting the aerosol from the cell by a pressure gradient.[15] As a further modification, numerical simulations by Lindner et al. on the HEAD cell led to the elimination of the back flow phenomenon in the aerosol uptake. These simulations explained the strategy to obtain a peak duration of less than 10 ms.[16] Similarly, an open noncontact cell with parallel LA plume-gas flow geometry was developed by Asogan et al.[17] However, their simulation work revealed that despite a calculated washout of <100 ms, such a performance was difficult to achieve experimentally due to the negative influence of connecting tubing, gas valves, and other flow impedances.[18]

A second design strategy is based on aerosol ejection orthogonal to the carrier gas flow. Gurevich et al. demonstrated a length-adjustable LA cell. This system yielded a fast washout of less than 100 ms, but only when the ablation location was chosen to be near to the outlet. The authors suspected a suppressed turbulence flow pattern around the ablation spot close to outlet being the reason for the observed fast washout.[19] Furthermore, Fricker et al. presented a large ablation cell capable of mounting large samples. The optimized gas flow at the ablation site was perpendicular to the ablation plume generation, and a restricted effective volume for the aerosol expansion guaranteed a washout of few seconds.[20]

While the first two design principles target the optimization of the cell geometry, the third principle attempts to improve the aerosol extraction scheme. Normal circular ablation cells[21] use only a pressurized inlet to push the aerosol through a gas outlet out of the cell. In contrast, the HEAD cell is based on a "venturi" extraction, which provides an additional force for a dense and fast extraction of the aerosol into the transport tube.[15,16]

Despite the development effort mentioned, most of the routinely applied ablation cells have an experimental washout time on the order of a few seconds for a 99% intensity drop from the peak maxima.[17,20,22] Only a few examples reported the washout time to be as short as 100 ms.[14,19] However extensive simulation studies have suggested that further improvement of the practical performance are possible.[16,18]

LA-ICP-MS Data Processing and Deconvolution. Simultaneous to the pioneer imaging work carried out using LA-ICP-MS, Kindness et al. integrated peak areas based on pulse signals in raster scanning, which would be the most suitable approach for image reconstruction. Since the peaks were well separated (no overlap), the washout was not interfering with successive ablations. However, the total imaging time was extended due to the tens-of-second peak duration.[5] Most of the LA-based imaging studies reported have not been based on single shot ablations, but employed (seemingly) fast imaging at higher ablation frequencies instead. In a few studies, a data deconvolution scheme was applied to compensate for the signal overlap from previously ablated shots in the continuous line scan.[23] A prerequisite for this correction is to describe theoretically the single shot transient signal, for example, as derived and reported by Bleiner et al.[24] and Plotnikov et al.[9]

The present study was focused on the development of a fast washout ablation cell for high spatial resolution chemical imaging and its applications to both sequential and simultaneous MS instruments. The new LA cell concept is based on fundamental knowledge about laser-generated aerosol expansion[25] with the goal of delivering the aerosol into the fast

flow channel of the carrier tube while keeping an undisturbed laminar flow pattern within the transport system. The resulting tube cell presented here was experimentally tested using single shot laser ablations. Furthermore, imaging capabilities were demonstrated by analyzing microstructured metallic thin film samples and a breast cancer tissue thin section at high spatial resolution.

EXPERIMENTAL SECTION

Tube Cell Design. A laser ablation cell contains the sample(s) and transports the laser-generated aerosol through tubing in a carrier gas to the ICP. Any type of ablation cells inserted into the pathway will disturb the carrier gas flow pattern and will influence the signal dispersion. Such negative effects can be minimized by using a section of the tubing as a "tube-like" cell. The tube cell has the same inner diameter as the tubing for aerosol transport to the ICPMS but is modified to allow introduction of the laser-generated aerosol into the carrier gas. In this study, a rectangular cuboid cell, made of acrylic glass [poly(methyl methacrylate), PMMA] was placed between the transport tubes. A 3 mm inner diameter hole was machined into the acrylic glass along the long axis. On the top side of the cell, a UV transparent silica window was fixed, and on bottom side a small hole was drilled, which allows the laser-generated aerosol to enter the carrier gas flow. The sample was mounted in a container attached to the cell top, typically spaced 350 μm (unless otherwise stated in the text) from the carrier tube bottom opening. For large samples, the cell container volume can be manufactured accordingly. An additional gas inlet was connected to provide a sheath gas flow through the bottom hole of the tube cell. A schematic cross-section view of the tube cell is shown in Figure 1. In the studies, Ar carrier gas

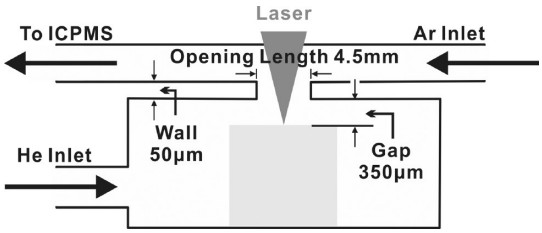

Figure 1. Cross-section sketch of a tube cell, not to scale.

passed through the tubing and a He sheath gas was introduced from the inlet on the container. Adding He from the sample container has three advantages: (i) this setup flushes the aerosol parallel to the aerosol ejection direction, which facilitates the uptake of the particles; (ii) He gas forms a "protected" region above the sample surface and ensures that the ablation is conducted under a low viscosity atmosphere;[25,26] (iii) the mixed Ar and He in the tube cell negates the need for a dispersive gas adapter (Ar/He mixing bulb) at the entrance of the ICP. Furthermore, both flow velocities and gas viscosity are increased compared with systems using only He as the carrier gas, which further reduces aerosol dispersion. The tube cell was mounted on a motorized XYZ-stage for automatically controlled applications.

Setup for Tube Cell Optimization, Performance Evaluation, and Characterization. A 193 nm ArF excimer laser system (Lambda Physik, Göttingen, Germany) with a homogenized laser beam profile was coupled to an Agilent 7500cs ICP-quadrupole-MS instrument (ICP-QMS, Agilent Technologies, Waldbronn, Germany). Laser fluence used in the experiments was adjusted to 17.3 J/cm^2. In order to improve the confidence level, all data points were derived from 3 × 3 single shot matrix scans (unless otherwise stated) with a laser spot size of 10 μm and a spacing of 15 μm between adjacent shots. Three millimeter inner diameter PTFE (polytetrafluoroethylene) tubing was used for the Ar and He inlets and the mixed-gas outlet (Figure 1). The argon carrier gas was set to 1.1 L/min. The helium sheath gas was provided to the cell at a flow rate of 0.6 L/min. The 50 cm long outlet tubing was directly connected to the ICP torch without changing the inner diameter. The tube cell performance measurements were carried out using a dwell time of 10 ms.

The optimization included an adjustment of the following system independent parameters: (i) the distance between the carrier tube opening and the sample surface; (ii) the Ar carrier gas flow rate; (iii) the He sheath gas flow rate. When the impact of one parameter was investigated, the other two were set to the "preoptimized" conditions (gap distance of 350 μm, Ar flow at 1.1 L/min, He flow at 0.6 L/min; see Figure 2). These conditions were determined from preliminary tunings by maximizing the peak height and minimizing washout of the online transient signals when a 10 μm laser spot was ablated on the glass NIST610 using 1 Hz line scan.

In order to describe the washout of the cell, single isotope ^{27}Al acquisitions during 1, 10, and 30 Hz laser ablations on NIST610 standard reference material (SRM) were performed (Figure 3) under the optimized conditions. The washout of each LA peak was characterized using height criterion[27] and compared in peak width, which is determined by the full width at 1% maximum (FW0.01M). The ICP was operated at 1470 W, and the quadrupole MS was set to one point per peak in peak hopping mode.

The data were evaluated based on a normalized peak width, which is the peak width divided by the total counts collected within each peak (peak area).

The characterization of the cell for routine analysis was carried out using the same parameters as described above. However, multiple isotopes from low and mid to high masses were recorded in different runs. Peak height sensitivities and peak area sensitivities were abundance corrected, in order to demonstrate the trend of the sensitivity with respect to masses. Limits of detection (LOD) were estimated from the ratio of 3σ of background signals to the peak height sensitivities (see Figure 4). The usage of peak height sensitivity instead of peak area sensitivity in LOD calculation was added for comparison to the conventional setup.

Microstructured Metallic Thin Film Patterns Preparation for High Spatial Resolution Imaging. The samples used for demonstrating imaging capabilities were produced by a laser-induced forward transfer (LIFT) method, which is a positive direct-write depositional process, meaning that the spatial pattern is created by adding material to the substrate, rather than removing material. The LIFT method is explained in depth elsewhere,[28,29] as well as in the Supporting Information. Two patterns were produced in different deposited material combinations, either a 60 nm thick Au "ETH" thin layer on bottom and an 80 nm Ag "PSI" on top (Au/Ag) or an 80 nm thick Al "ETH" thin layer on bottom and an 80 nm Ag "PSI" on top (Al/Ag). To validate the deposition process by scanning electron microscopy (SEM), a 5 nm Pt thin film was uniformly coated on the microstructured thin film pattern of Au/Ag, but not on that of Al/Ag. The corresponding

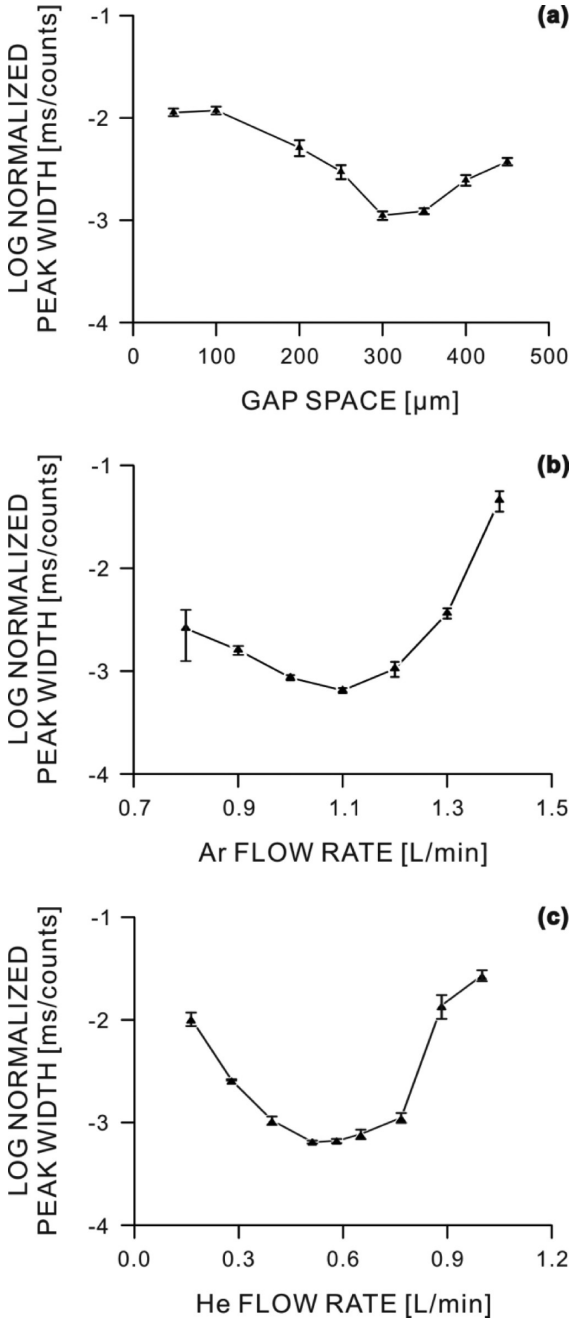

Figure 2. Tube cell optimization on various parameters: (a) gap width between opening of the tube cell and sample surface; (b) Ar carrier gas flow rate; (c) He sheath gas flow rate, demonstrated by ^{27}Al signal from laser ablations using 10 μm spot size on NIST610 SRM. Peak width in milliseconds is normalized to peak area in counts based on full width at 1% maximum criterion. *Y* axes indicate the order of magnitude.

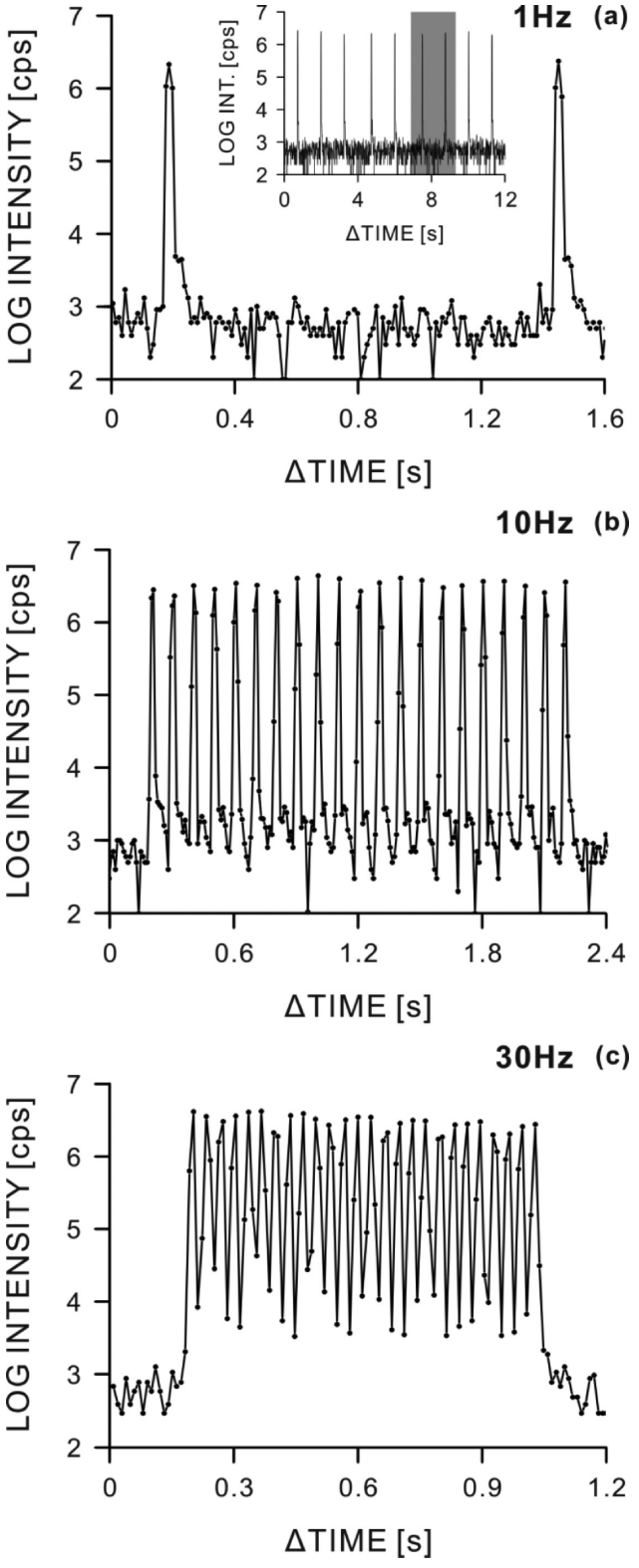

Figure 3. Performance of the tube cell demonstrated by ^{27}Al intensity in NIST610 SRM using a laser spot size of 10 μm at various LA frequencies: (a) ~1 Hz transient signal; (b) 10 Hz transient signal; (c) 30 Hz transient signal. *Y* axes indicate the order of magnitude. Note that the displayed "Time" axes are in relative scale, not absolute time intervals.

optical microscope and SEM images are shown in Figure 5a,b for the Au/Ag pattern, and the optical microscope images of the Al/Ag pattern are shown in Figure S-2a,b, Supporting Information.

Instrumentation and Operating Conditions for Imaging of Microstructured Metallic Thin Film Pattern with Au/Ag. A laboratory-based X-ray fluorescence system (laboratory-based XRF, ORBIS microXRF analyzer, EDAX Inc.) was used to acquire an image of the coated sample. The ORBIS system was equipped with a Rh cathode, operated at 40 kV and 1000 mA. An X-ray beam size of 30 μm was delivered by means of a polycapillary lens onto the sample area. The beam stepping

dx.doi.org/10.1021/ac400996x | *Anal. Chem.* 2013, 85, 10107−10116

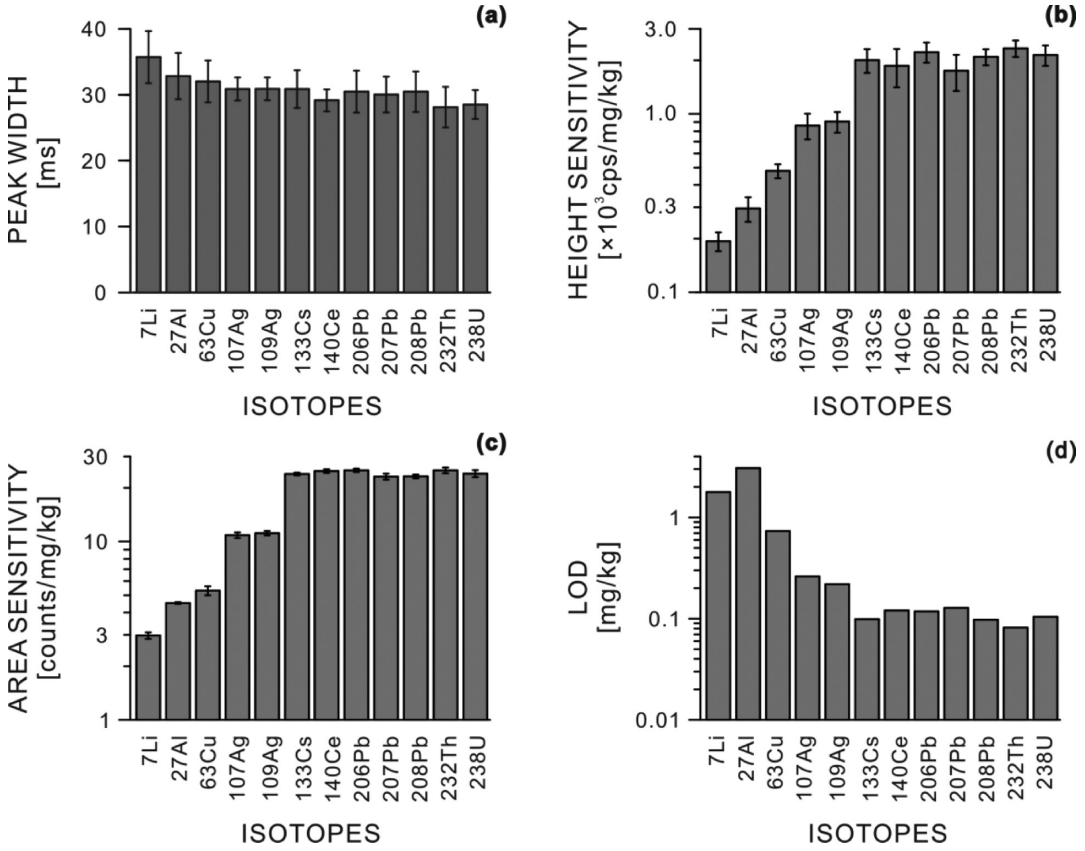

Figure 4. Tube cell performance characterizations on (a) peak width, (b) abundance normalized sensitivities calculated from peak height, (c) abundance normalized sensitivities calculated from peak area, and (d) limits of detection (LOD) calculated from part b. All performances were derived from nine single spot laser ablation measurements on NIST610 SRM. Peak width and peak area were calculated based on full width at 1% maximum criterion.

was ∼4 μm in the horizontal direction and ∼3 μm in the vertical direction. Each pixel was integrated for 0.5 s. During measurements, the sample chamber was kept under vacuum conditions in order to minimize the absorbance of the low-energy fluorescence photons by air. A 25 μm thick Ti filter was applied to the incident X-ray beam to reduce background contributions.

Synchrotron-radiation-based micro-X-ray fluorescence (SR-microXRF) was employed for high spatial resolution measurements. Measurements were conducted at the microXAS beamline of the Swiss Light Source (SLS). The excitation beam of 17.9 keV was delivered by an in-vacuum insertion device and monochromatized by a double-crystal monochromator using a Si(111) crystal pair. The beam was further focused to ∼1 μm by a pair of reflective mirrors in the Kirkpatrick–Baez arrangement. Sample area was continuously scanned (on-the-fly) with a pixel size of 1 × 1 μm^2 (image size 852 × 370 μm^2). A single-element Si drift diode energy-dispersive X-ray (EDX) spectrometer (Ketek) collected the fluorescence spectra. Integration time per pixel was 200 ms.

In the current imaging experiment, LA-ICP-MS is a destructive technique and was therefore applied for imaging after analyzing the samples by the two XRF techniques. The same configuration as described for the tube cell characterization was used, with the exception of a reduced laser fluence of 15.7 J/cm^2. An area of 852 × 408 μm^2 was analyzed by combining line scans (from left to right, and multiple line scans from top to bottom of Figure 5c,d). The laser pulse rate was set to 10 Hz. The distance between successive laser shots and the lateral distance between line scans was 4 μm in both cases, based on a 4 μm laser crater. The actual laser beam size was 1–2 μm, but a larger affected region was observed, which can be explained by an enlarged heat penetration volume (high thermal diffusion in the metallic thin films and nanosecond light–material interaction time). Three isotopes, ^{107}Ag, ^{195}Pt, and ^{197}Au, were measured in peak hopping mode with a dwell time of 600 μs for each isotope. However, due to an instrument quadrupole-settling time of a few milliseconds for each isotope, the reading of an entire set of isotopes could not be completed in less than 10 ms. Obviously, such a large overhead fraction (low duty cycle) does limit signal quality obtainable during fast, high resolution imaging experiments. Data analysis was based on the integration of each single shot signal.[5,23]

Biological Tissue Sample Preparation. A formalin-fixed paraffin-embedded human epidermal growth factor receptor 2 (HER2)-enriched breast cancer tissue was sectioned to a thickness of 6 μm. The sample was processed on a Discovery XT platform (Ventana Medical Systems) under CC1m epitope recovery conditions. Afterward, the sample was blocked for 30 min with phosphate-buffered saline (PBS)/1% bovine serum albumin (BSA)/0.1% Triton X and then incubated with 200 μL ^{165}Ho-tagged anti-HER2 antibody at 5 μg/mL for 50 min. The sample was washed three times with PBS/0.1% Triton X and dried at room temperature. For antibody conjugation with ^{165}Ho, a commercial MAXPAR antibody labeling kit (DVS Sciences, Canada, http://www.dvssciences.com/labeling-reagents.php) was employed. After sample preparation, the

dx.doi.org/10.1021/ac400996x | Anal. Chem. 2013, 85, 10107–10116

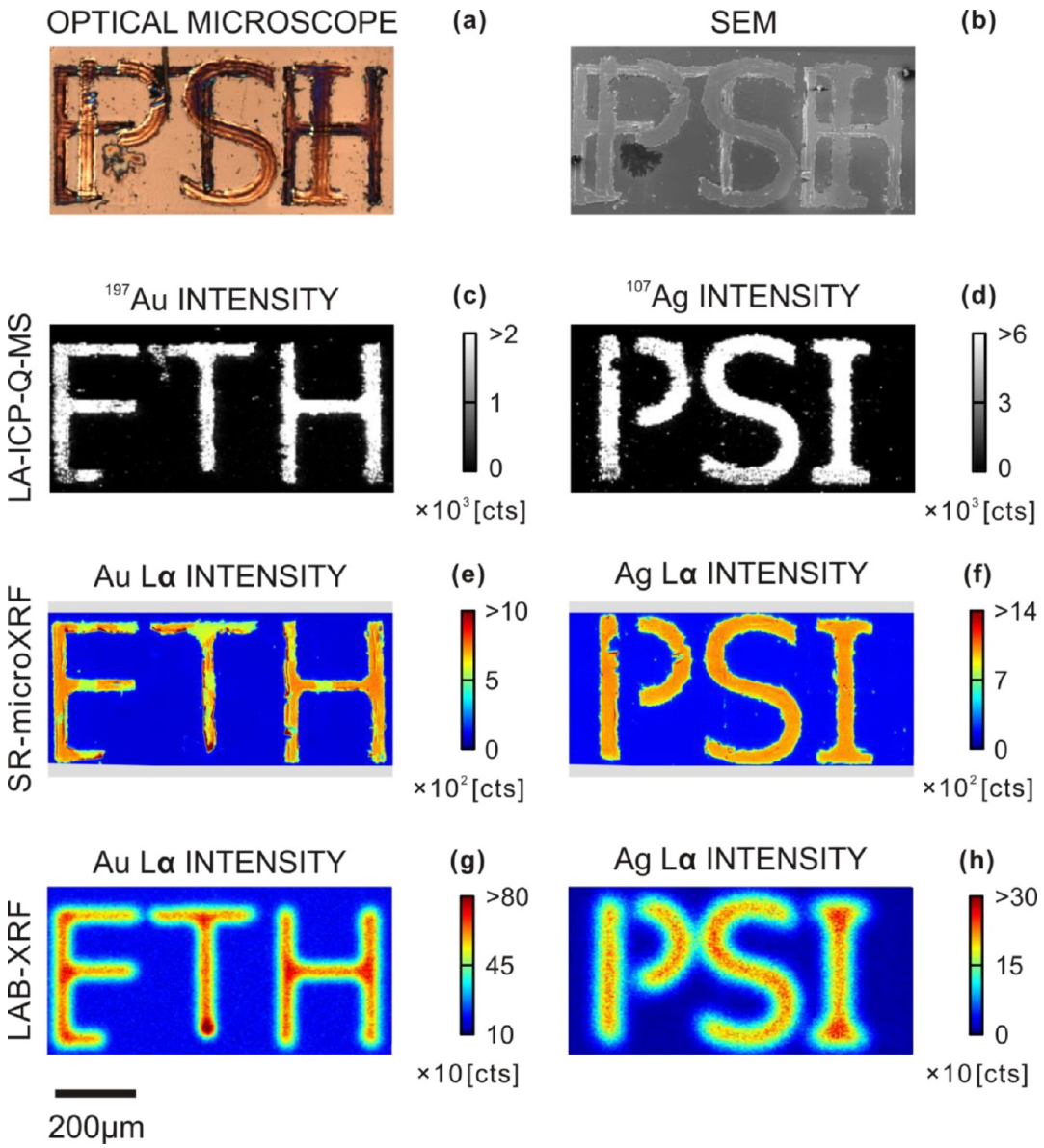

Figure 5. A Pt coated microstructure metallic thin film pattern with Au "ETH" thin film on bottom and Ag "PSI" thin film on top was imaged by (a) optical microscopy, (b) secondary electron image using scanning electron microscopy, (c, d) high spatial resolution tube cell equipped LA-ICP-quadrupole-MS, (e, f) 1 μm high spatial resolution SR-microXRF, and (g, h) laboratory-based microXRF.

sample thickness shrunk to only a few hundreds of nanometers (results by white light interferometry not shown).

Instrumentation and Operating Conditions for Tissue Imaging. Tissue imaging was conducted on an Element2 (Thermo Fisher Scientific) ICP-MS coupled to the tube cell equipped ArF excimer laser ablation system with 1−2 μm laser spot size (4 J/cm^2). This laser fluence is sufficiently high to ablate through the tissue thin section within one laser shot but ablation on the glass substrate was not observed. The operating conditions were optimized for maximum sensitivity of fast transient signals. Therefore, only ^{165}Ho was recorded during tissue ablation. For imaging, the sample was scanned line by line at a laser frequency of 20 Hz (raster), and an image pixel size of 1 × 1 μm^2 was achieved. The dwell time of the MS was set to 50 ms, in accordance to the laser frequency applied.

RESULTS AND DISCUSSION

Tube Cell Optimization. The dependence of the dispersion on the gap between the tube cell bottom and the sample surface is depicted in Figure 2a. The plotted peak widths were normalized to the total counts collected in FW0.01M. A minimum peak width at a gap width of 300−350 μm was observed. Using this optimized gap distance, the Ar and He gas flow rate optimizations were carried out. The corresponding results are shown in Figure 2b,c based on the normalized peak widths. All three optimizations yield an evident minimum of ∼10^{-3} ms/count for the normalized peak width. All measurements reported in the following sections were conducted using these optimized values for sample gap and gas flow rates. Depending on different setups, such optimization values may vary.

Performance Evaluation of the Tube Cell on the Laser Ablation System. The dispersion behavior of the tube cell was characterized using a laser frequency of ∼1 Hz, and typical

dx.doi.org/10.1021/ac400996x | Anal. Chem. 2013, 85, 10107−10116

transient signals (shown in logarithmic scale) are summarized in Figure 3a and insert. The FW0.01M of a single laser pulse signal of a major element lasted around 30 ms. The peak height and peak area were calculated to be $(2.3 \pm 0.2) \times 10^6$ cps and $(4.2 \pm 0.1) \times 10^4$ counts, respectively. The transient peak has a slightly asymmetric shape, tailing slightly, which is caused by delayed washout of the aerosol. After the peak maxima, signals dropped more than 2 orders of magnitude within 20 ms. This time interval contained more than 99.6% of the total signal. The residual fraction of the total signal (0.4% integrated signal area) was found in the tail of the peak which reached background after 40−50 ms. The slope of the second signal decay is shallower than that for the fast washout, indicating a different process, which is suspected to be related to the uptake of redeposited material from the surface. This is most likely due to the flow of the He sheath gas into the tube cell bottom opening, which is parallel to the laser plume injection that flushes the area around the crater most efficiently. Spacing the single shots by 1 s indicates that no further sample removal occurs after the second signal decay process (see Figure 3a).

Figure 3b shows the transient signal acquired at a laser frequency of 10 Hz. The peak width and shape were similar to those signals measured at 1 Hz. However, the peak maxima oscillate around an average value of $(3.3 \pm 0.5) \times 10^6$ cps (and average peak area of $(5.7 \pm 0.3) \times 10^4$ counts). The oscillating artifact is probably caused by aliasing. The relative standard deviation of the peak maxima was determined to be 15%, and that of the peak areas was approximately 5%.

Figure 3c illustrates a transient signal obtained at a laser frequency of 30 Hz. The width and shape of the peak were similar to the signals measured at 1 and 10 Hz. The average values for peak height and peak area are $(3.1 \pm 0.7) \times 10^6$ cps and $(5.6 \pm 1.9) \times 10^4$ counts, respectively. The aliasing effect remains similar to the 10 Hz conditions (compare Figure 3b,c). The signal structure indicates that two adjacent peaks cannot be separated to background from each other. However, the overlap between two successive peaks is less than 1% of the peak maximum. Therefore it can be concluded that even ablation at 30 Hz would allow the imaging of concentration differences as large as 2 orders of magnitude, which makes this ablation cell geometry very attractive for fast high spatial resolution LA imaging over large concentration ranges. The entire evaluation demonstrates that the washout is significantly improved, resulting in a peak width (FW0.01M) as short as 30 ms. However, the investigations show also that simultaneous detection, for example, using a ICP-Mattauch−Herzog-MS (ICP-MH-MS)[30,31] or ICP-TOF-MS,[5,13,32] would be highly beneficial, because it would improve acquisition speed further, and aliasing effects in the raw data would be absent.

Analytical Characterization of the Tube Cell. The analytical characterization of the tube cell performance is documented in Figure 4. Peak widths, sensitivities calculated from peak heights and peak areas, and limits of detection (LOD) are shown for different isotopes from low m/Q (^{7}Li) to high m/Q (^{238}U). In Figure 4a, the mean peak widths of all isotopes measured are given, and they are in a narrow range of 30−35 ms. The reported signal durations were calculated based on FW0.01M. The standard deviations across the m/Q range are the result of shot-to-shot variations concerning the ablated mass, aliasing effects, and fluctuations due to instabilities in the gas flow dynamics.

Figure 4b shows the normalized sensitivities for the peak maxima (given in cps mg^{-1} kg), which were determined using 10 μm craters in a single shot ablation mode. Compared with commonly used ablation cell setups in single shot mode, the peak height sensitivities were improved by a factor of 10 (Supporting Information, Figure S-1). This improvement is not due to an enhanced sample transport efficiency or superior ionization but is entirely based on preserving the sample aerosol density from the ablation site to the ICP. A relatively high standard deviation (RSD $\approx$ 15%) of the normalized sensitivities of peak heights was observed for all m/Q. This variability is caused mainly from the aliasing effect in the sequential MS operation. This conclusion is further supported by the figures of merit of the integrated peak areas. As demonstrated in Figure 4c, the RSD of the peak area sensitivities have typical values of approximately 5% across the entire mass range and are more stable than that of peak height sensitivities.

The limit of detection (LOD) is a useful figure of merit to compare the performance of different analytical systems or procedures. Commonly, three times the standard deviation of the background criterion is used to state the minimum detectable background-corrected net concentration. For the tube cell LA-ICP-MS setup using single laser shot of a 10 μm spot, all of the interested isotopes show LODs around or below 1 mg/kg (Figure 4d). Heavy isotopes are less influenced by the space charge effect;[33] hence their LODs around 0.1 mg/kg are better than light masses. In theory, calculations using the low RSD peak areas would be more accurate. However it is more convenient to compare the current figures of merit to those from other setups; therefore LOD calculations were carried out in the conventional method, calculated from (mean of) peak height values in the unit of cps. LOD comparison between the tube cell and the conventional setup using a normal circular LA cell is shown in Supporting Information.

Fast Imaging of a Microstructured Thin Film Pattern of Au/Ag by Sequential Quadrupole-MS. The "ETH/PSI" pattern of Au/Ag was analyzed using various imaging techniques. The microscopic structural details of the pattern were imaged using optical microscopy (Figure 5a) and scanning electron microscopy (SEM, Figure 5b). These images were used to evaluate the microscopic chemical imaging capabilities of the high sensitivity, high spatial resolution LA-ICP-MS (Figure 5c,d). In order to demonstrate the improved imaging performance, the elemental images obtained using LA-ICP-MS are compared with images acquired using routinely applied high spatial resolution SR-microXRF (~1 μm^2 spot size, Figure 5e,f).

The optical and SEM images indicate that the thin film patterns were not perfect in terms of homogeneity, shape, and geometry. However, the spatial defects in these samples were considered to be well suited to be analyzed by these microprobe techniques to evaluate their capabilities to resolve small features. Generally, both LA-ICP-MS and SR-microXRF produced consistent images with sharp pattern boundaries. The rapid signal change from the thin film to background (or vice versa) was suggested as an indicator of high spatial resolution.[4] Similar details of selected microscopic features such as a void in the middle horizontal stroke of "E" (right end) or a separated dot at the top inner part of the right arm of "H" indicate that the resolving power of LA-ICP-MS is comparable to the 1 μm spatial resolution of SR-microXRF. An inconsistent feature on the left arm of the "T" between Figure 5c (LA-ICP-MS) and Figure 5e (SR-microXRF) was due to a scratch, inadvertently introduced during sample transportation from one laboratory

to another, which was captured by the optical microscope image in Figure 5a. In the SR-microXRF image (Figure 5e), a systematic heterogeneity on the "ETH" (Au) was caused by the "masking" effect from the "PSI" (Ag) pattern on top. This corresponds to a limitation in the quantification using SR-microXRF, which was mentioned previously.[34] In the case of stratified samples, systematic quantification uncertainties are introduced, even if mathematical corrections and algorithms could be employed to approximate the mean composition. An accurate quantification would require a priori knowledge regarding stratification structure of the sample.

This thin film pattern was also imaged on a conventional laboratory-based XRF system, which is considered as a powerful laboratory-scale technique for chemical imaging. As shown in Figure 5g,h, the coarse features with blurry boundaries were still visible and similar to the images made with the other techniques. However, the fine structures were not resolved, not even the big defects on the left side of the "P". It is important to note that spatial resolution is not primarily a function of the step size but of the "primary" beam size used. Secondary phenomena such as signal dispersion (LA-ICP-MS) or penetration (SR-microXRF) also limit the effective spatial resolution.

In addition to the spatial resolution of the images, the measurement time is another important figure of merit for the imaging technique. Among different systems and setups, it is useful to compare the time required per spatially resolved pixel. In the current setup, the SR-microXRF integration time was 0.2 s for each 1 × 1 μm^2 pixel, while the lab-based XRF required tens of seconds to acquire each 30 × 30 μm^2 spatially resolved pixel. When using LA-ICP-MS with the fast washout tube cell, the time per spatially resolved pixel was 0.1 s, similar to that of SR-microXRF, but with a higher sensitivity.

There are some important restrictions of the current LA-ICP-quadrupole-MS setup that limit elemental imaging. In multielement mapping, the short transient signals generated results with significant aliasing and spectral skew artifacts, resulting in "noisy" images (high RSD) even when investigating chemically homogeneous samples. Silver and gold images showed aliasing and spectral skew effected heterogeneities. In the qualitative representation (Figure 5c,d), the top limits of the gray color bars were only ∼1% of the maximum intensity. Furthermore, the short transient signals also restrict the number of elements that can be measured during the duration of the signal pulses. Considering the short pulse duration of a few tens of milliseconds and the overhead time for isotope switching (quadropole settling time of a few milliseconds), only a limited number of isotopes can be analyzed per single shot pixel.

The limited imaging capabilities can be improved by utilizing simultaneous isotope detection instrumentation. In order to demonstrate the advantage of such systems, a microstructured thin film pattern with Al and Ag was chemically imaged by ICP-Mattauch–Herzog-MS. More details are discussed in the Supporting Information in Figures S-2 and S-3. With the achievement of multi-isotope acquisition, many scientific applications would benefit from the novel high spatial resolution feature of tube cell LA-ICP-MS. Examples may include structured thin films deposited on electronic devices, contaminant diffusion in geological samples, or elemental distribution in geological archives related to climate changes.

Biological Tissue Thin Section Imaging. Among the many possible applications of our developed elemental imaging LA-ICP-MS system, we chose to demonstrate its potential by investigating biomarker distributions in a biological tissue thin section. Such analyses demand, first, micrometer resolution, to resolve the morphology of and to localize biomarkers in their compartments in the smallest biological unit, the cell. This information is crucial in the study of biological processes and for comprehensive diagnostic purposes. A second requirement is a minimized measurement time per pixel. In biological and biomedical analyses typically a large number of samples and large tissue areas (500 × 500 μm^2) need to be analyzed for statistical purposes. To demonstrate the feasibility of the designed ablation cell, a breast cancer tissue section was analyzed to investigate the human epidermal growth factor receptor 2 (HER2) status of individual cells illustrated in Figure 6. The image showed HER2 protein highly expressed on the cell membrane. HER2 is a major determinant of relapse free survival time, time to metastasis, and overall survival time after an initial breast cancer diagnosis. In the analysis, we achieved ∼1 μm spatial resolution. Such high spatial resolution and chemical sensitivity allowed a highly precise HER2 determination in the breast cancer tissue.

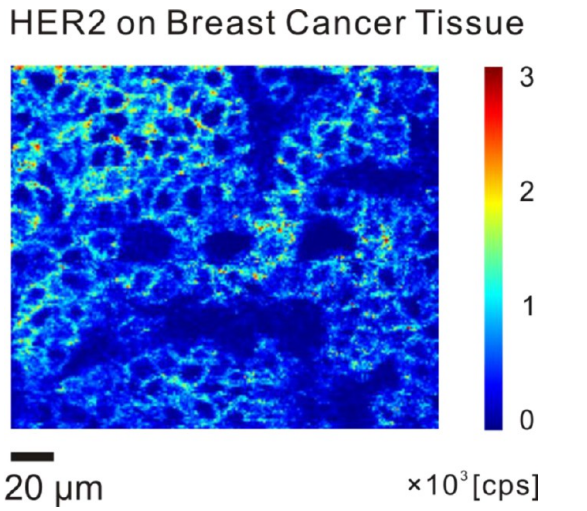

Figure 6. Human epidermal growth factor receptor 2 (HER2) distribution in a breast cancer tissue section was imaged by LA-ICP-single-detector-sector-field-MS.

The same sample has been probed using 1 μm^2 X-ray beam on the microXAS SR-microXRF facility of the SLS. However, as a consequence of the low trace metal tag (Ho) concentration on HER2 and severe interference with Fe in the XRF spectrum, the Ho signals were below the LOD. This case convincingly documents the superior sensitivity of a LA-ICP-MS equipped with the new tube cell for chemical imaging in micrometer-scale spatial resolution.

CONCLUSION

A fast washout laser ablation cell for high spatial resolution high sensitivity imaging was developed and evaluated. This has improved the already versatile and sensitive LA-ICP-MS technique as a microscopic chemical imaging tool. The study included the optimization, characterization, and figures of merit of this novel LA tube cell, as well as its imaging applications on engineered materials and on a biological tissue sample. Single shot transient signals on NIST610 were achieved with pulse widths of 30 ms (FW0.01M) using a 10 μm focused laser beam.

This fast washout (low aerosol dispersion) was observed for low, mid, and high mass isotopes. The sensitivity and LOD in single laser pulse mode were superior to those of conventional LA setups.

In a case study, microstructured metallic thin film patterns were elementally mapped to demonstrate the imaging capabilities of the tube cell LA system coupled to a sequential ICP-quadrupole-MS or a simultaneous ICP-Mattauch–Herzog-MS. The high spatial resolution images obtained using LA-ICP-MS are similar to those in SR-microXRF images with a spatial resolution of 1 μm. Furthermore, a higher normalized pixel intensity was obtained in the LA images. The agreement of the images increases the reliability of applying both techniques as complementary analytical methods, allowing a robust cross-validation and cross-calibration.[23,34] This technique could be useful for studying quantitative high spatial resolution elemental migrations in geological or environmental samples or elemental determinations in thin film coatings for optical and electronic devices.

In this work, the proof-of-principle imaging case study on a biological tissue sample using LA-ICP-MS was described. The resulting distribution of the HER2 biomarker in a breast cancer tissue thin section was achieved with a subcellular resolution (~1 μm) by employing the novel laser ablation cell. The cell-membrane-bonded-HER2 distribution showed a good conformity with biological knowledge. Moreover, spatially resolved multiplexing biomarker distributions in breast cancer tissue thin sections can be thoroughly investigated using the same tube cell LA setup coupled to a simultaneous ICP-TOF-MS (CyTOF, DVS Science, Canada). Such an advanced multiparameter imaging tool can assist biologists in studying cancer and other diseases, help pathologists better classifying their patients, and help pharmacologists developing tailored drugs.

Nevertheless, the LOD of LA-ICP-MS is approached when a ~1 μm laser spot is used with the tube cell. A current limitation is the sensitivity (signal per unit concentration) of the ICP-MS. Despite many efforts, the design and construction of an advanced system for ionization of the aerosols ablated at atmospheric pressure and the efficient introduction of the generated ions into a mass analyzer are remaining challenges.

■ ASSOCIATED CONTENT

Supporting Information

Additional information as noted in text. This material is available free of charge via the Internet at http://pubs.acs.org.

■ AUTHOR INFORMATION

Corresponding Authors

*E-mail: daniel.grolimund@psi.ch. Fax: +41 56 310 4551.

*E-mail: guenther@inorg.chem.ethz.ch. Fax: +41 44 633 1071.

Present Address

▽J.R.H.S.-S.: Grant Institute, University of Edinburgh, Edinburgh EH9 3JW, U.K.

Notes

The authors declare no competing financial interest.

■ ACKNOWLEDGMENTS

Roland Mäder from the LAC workshop at ETH Zurich is greatly appreciated for manufacturing of the LA cell. We acknowledge the provision of access to research facilities in the Materials Group, General Energies Department, Paul Scherrer Institute (PSI), for preparing the thin film samples. Cécile Marichal from PSI is acknowledged for her expert help in acquiring SEM images. Dr. Anna Maria Krzton-Maziopa from PSI is thanked for the introduction to the ORBIS XRF instrument. The authors acknowledge the internal support from the research group of Trace Element and Micro Analysis at ETH Zurich. We thank Prof. Dr. med. Peter Wild at University Hospital in Zurich for providing the breast cancer thin tissue and Martina Storz for cutting the sample. A part of the experiments were performed on the microXAS beamline at the Swiss Light Source, Paul Scherrer Institut, Villigen, Switzerland. Financial support by the Swiss National Foundation is also acknowledged (Project 200021_119779 and Project 31003A_143877). B.B. is supported by a Swiss National Science Foundation (SNF) Assistant Professorship Grant (No. PP00P3_144874). Thanks to Henry Longerich for comments and a detailed edit of the document.

■ REFERENCES

(1) Gray, A. L. *Analyst (Cambridge, U. K.)* **1985**, *110*, 551–556.
(2) Günther, D.; Hattendorf, B. *TrAC, Trends Anal. Chem.* **2005**, *24* (3), 255–265.
(3) Chenery, S.; et al. *Chem. Geol.* **1995**, *124* (1–2), 55–65.
(4) Woodhead, J. D.; et al. *Geostand. Geoanal. Res.* **2007**, *31* (4), 331–343.
(5) Kindness, A.; Sekaran, C. N.; Feldmann, J. *Clin. Chem. (Washington, DC, U. S.)* **2003**, *49* (11), 1916–1923.
(6) Hutchinson, R. W.; et al. *Anal. Biochem.* **2005**, *346* (2), 225–233.
(7) Jackson, B.; et al. *Anal. Bioanal. Chem.* **2006**, *384* (4), 951–957.
(8) Becker, J. S.; et al. *Anal. Chem.* **2005**, *77* (10), 3208–3216.
(9) Plotnikov, A.; Vogt, C.; Wetzig, K. *J. Anal. At. Spectrom.* **2002**, *17* (9), 1114–1120.
(10) Bleiner, D.; Bogaerts, A. *Spectrochim. Acta, Part B* **2007**, *62* (2), 155–168.
(11) Tanner, M.; Günther, D. *J. Anal. At. Spectrom.* **2005**, *20* (9), 987–989.
(12) Tanner, M.; Günther, D. *J. Anal. At. Spectrom.* **2006**, *21* (9), 941–947.
(13) Tanner, M.; Günther, D. *Anal. Bioanal. Chem.* **2008**, *391* (4), 1211–1220.
(14) Leach, A. M.; Hieftje, G. M. *Appl. Spectrosc.* **2002**, *56* (1), 62–69.
(15) Pisonero, J.; Fliegel, D.; Günther, D. *J. Anal. At. Spectrom.* **2006**, *21* (9), 922–931.
(16) Lindner, H.; et al. *J. Anal. At. Spectrom.* **2010**, *25* (3), 295–304.
(17) Asogan, D.; et al. *J. Anal. At. Spectrom.* **2009**, *24* (7), 917–923.
(18) Asogan, D.; et al. *J. Anal. At. Spectrom.* **2011**, *26*, 631–634.
(19) Gurevich, E. L.; Hergenroder, R. *J. Anal. At. Spectrom.* **2007**, *22* (9), 1043–1050.
(20) Fricker, M. B.; et al. *Int. J. Mass Spectrom.* **2011**, *307* (1–3), 39–45.
(21) Hattendorf, B. Ion Molecule Reactions for the Suppression of Spectral Interferences in Elemental Analysis by Inductively Coupled Plasma Mass Spectrometry, Diss. Eth No. 14926, ETH Zurich, Zurich, Switzerland, 2002.
(22) Müller, W.; et al. *J. Anal. At. Spectrom.* **2009**, *24* (2), 209–214.
(23) Wang, H. A. O.; et al. *Anal. Chem.* **2011**, *83* (16), 6259–6266.
(24) Bleiner, D.; Günther, D. *J. Anal. At. Spectrom.* **2001**, *16* (5), 449–456.
(25) Koch, J.; et al. *Spectrochim. Acta, Part B* **2008**, *63* (1), 37–41.
(26) Horn, I.; Günther, D. *Appl. Surf. Sci.* **2003**, *207* (1–4), 144–157.
(27) Lindner, H.; et al. *Anal. Chem.* **2009**, *81* (11), 4241–4248.
(28) Shaw-Stewart, J. R. H.; et al. *Appl. Phys. A: Mater. Sci. Process.* **2011**, *105* (3), 713–722.
(29) Shaw-Stewart, J. R. H.; et al. *Appl. Phys. Lett.* **2012**, *100* (20), No. 203303.

(30) Schilling, G. D.; et al. *J. Anal. At. Spectrom.* **2010**, *25* (3), 322–327.
(31) Resano, M.; McIntosh, K. S.; Vanhaecke, F. *J. Anal. At. Spectrom.* **2012**, *27* (1), 165–173.
(32) Borovinskaya, O.; et al. *J. Anal. At. Spectrom.* **2013**, *28*, 226–233.
(33) Niu, H.; Houk, R. S. *Spectrochim. Acta, Part B* **1996**, *51* (8), 779–815.
(34) Wang, H. A. O.; et al. *Chimia* **2012**, *66* (4), 223–228.